ZAMBIA INFORMATION COMMUNICATION TECHNOLOGY (ICT) JOURNAL

Volume 7 (Issue 1) (2023) Pages 7-15

Synthetic Aperture Radar and Optical Sensor Techniques Using Google Earth Engine For Flood Monitoring and Damage Assessment – A Case Study of Mumbwa District, Zambia

Christopher Shilengwe
Geospatial Department
National Remote Sensing Centre
Lusaka, Zambia
shilengwe93@gmail.com

Faustin Banda
Director
National Remote Sensing Centre
Lusaka, Zambia
faustin.banda@unza.zm

Penjani Hopkins Nyimbili
Geomatic Engineering Department
University of Zambia
Lusaka, Zambia
penjani.nyimbili@unza.zm

Wallace Mukupa
Head of Department – Geomatic Engineering
University of Zambia
Lusaka, Zambia
wmukupa@unza.zm

Robert M'sendo
Head of Department – ICT Education
National Institute of Public Administration (NIPA)
Lusaka, Zambia
r.msendo@nipa.ac.zm

Turan Erden
Associate Professor - Geomatics Engineering Department
Istanbul Technical University
Istanbul, Turkey
erdentur@itu.edu.tr

Abstract - Radar and Optical based satellite sensors were used in the study of the Mumbwa flood of December 2020. The Synthetic Aperture Radar (SAR) based Sentinel-1B was processed in Google Earth Engine (GEE) and utilized to generate an image mosaic from December 2020 to May 2021 to delineate flood extent. A local water histogram threshold change detection approach by image ratio was utilized to determine the flood extent with an intensity value of 1.26 dB as it fitted the study area uniquely as opposed to the global value of 1.25 dB. After extracting the initial flood water extent, it was necessary to filter out regions which inundated during the flood period. This was carried out using the following datasets and parameters: The HydroSHEDS Digital Elevation Model (DEM) was used to filter out regions with a slope value of greater than 7% and the Global Surface Water Layer was used to clip out regions with existing permanent surface water. Once the flooded areas were identified, the Optical based Sentinel-2 was used in the production of a Land Use Land Cover (LULC) Map for August 2020 in order to superimpose the flooded areas with existing land features over the study area. The map also under went pre and post processing in GEE using the Random Forest Classification Algorithm that achieved an Overall Accuracy and Kappa Coefficient of 0.957 and 0.91519 respectively. Thereafter the flood analysis and damage assessment were carried out. The quantitative damages to Landcover were found to be: Wetland 6,338.97 Ha (33.27%), Shrubland 5,117.75 Ha (26.89%), Biochar Soil 3,660.47 Ha (19.21%), Trees 3,466.37 Ha (18.19%), Bare soil 273.47 Ha (1.44%), Crop Fields 190.69 Ha (1%) and Built-Up 4.13 Ha (0.02%). Therefore the use of SAR by local histogram threshold approach with Optical datasets for LULC map production proved successful in the study of flood damage.

Keywords - *Random Forest Algorithm, Synthetic Aperture Radar, Histogram Threshold, Google Earth Engine*.

I. INTRODUCTION

Inundation and flooding along open water bodies occur as a result of catchment overflow caused by increased rainfall or other factors. In general, over certain river sections, flooding is a seasonal occurrence that varies in extent and severity [1].

Flood damage that has serious repercussions may be classified as a disaster event, depending on the human impact. Flood disasters are a major concern in developing countries that lack Early Warning Systems and Mitigation measures [2].

In the analysis and delineation of flood events as well as general land resource mapping, remote sensing and specifically satellite imagery are growing areas of particular interest due to their public availability and relative capability in capturing large areas in a single image [3]. Multispectral and optical imagery such as the Landsat Collection has been used for various mapping studies inclusive of flooding but said datasets are limited due to their incapability to penetrate cloud cover and operation which is limited to day-time [4]. Active sensors such as Synthetic Aperture Radar (SAR) act as a remedy that can penetrate climate-related interferences such as cloud cover and can operate at night [5]. For flood analysis, it is of key importance to understand the terrain of the study area. For this, a Digital Elevation Model (DEM) must be incorporated into the workflow as floods tend to run off areas with relatively high slope values [6].

Processing of datasets for flood monitoring has been facilitated historically using various software vendors that offer continuous and unimpeded analysis tools. In recent years the development of cloud technologies has improved the outlook for remote sensing and data availability. Google Earth Engine (GEE) provides the said datasets as well as an Application Programming Interface (API) that allows for the seamless access and processing of Satellite Imagery Datasets [7].

This research used Sentinel-1 SAR data with a histogram thresholding approach on a local context to assess flood damage and impact over the study area [8]. Upon pre-processing the SAR data in unison with DEMs, a histogram fitting was carried out to delineate flood water from existing permanent open water in the study area for the 2020-21 rainy season [9]. A Change Detection (CD) approach using remote sensing is an accepted way to carry out a time series analysis using remote sensing datasets [10]. This study, therefore, used an image ratio CD approach with a local histogram threshold that is fitted specifically to the study area [11]. Thereafter a Land Use Land Cover (LULC) map using Sentinel-2 was generated using the Random Forest (RF) Classification Algorithm to serve as a study site for the flood impact assessments [12].

II. LITERATURE REVIEW

A. Related Works

Chini et al. [5] used a clustered split based histogram approach were they applied Change Detection (CD) in a SAR time series for flood delineation. The SAR backscatter was clustered into a local histogram threshold specifically tailored to the study area. However they did not factor in the effects of elevation on surface water runoff in their production of flood maps.

Muhadi et al. [6] explored the use of LiDAR derived DEMs in the workflow of flood analysis and emphasizes the inclusion of elevation data in delineating flood inundation.

In their research, Pandey et al. [25] utilizes SAR in GEE to monitor flood impact on agriculture and population in a flood prone basin. The backscattering coefficient, which is also known as sigma nought (σ0), is the normalized measure of the radar return from a distributed target and indicates the reflective intensity of a microwave object represented as the per unit area on the surface [15]. Their work used a global threshold of 1.25 sigma nought (σ0), in a CD by image differencing. They then went on to use The Gridded Population of the World (GPW) population density and Global Human Settlement Layer (GHSL) as well as The Copernicus Global land cover dataset that was acquired from the European Space Agency (ESA) for flood damage assessment [23]. This method though viable is not recommended as the use of a global LULC map for the designation and quantification of flood damage tends to import aggregated errors in the workflow from the classification on a global scale and this is a major drawback to this method.

Conde and Muñoz [1] in their study use a SAR RGB (RED+BLUE+GREEN) composite to visualize the temporal modifications of their study area and apply change detection. Their study observed that in the SAR composite histogram, flooded areas fall within the limits having the lower bound being -24 dB and the upper bound -21 dB, (-24 dB, -21 dB).

To carryout LULC classification, Xu et al. [4] used the classifiers, Support Vector Machine (SVM) and Random Forest (RF) to classify a Landsat-8 dataset over the study area which had a heterogeneous landscape. The overall accuracies they observed were (overall accuracy: 85.5%) for SVM and (overall accuracy: 86.2%) for RF. It was found that RF was more suitable than SVM for classifying Landcover without the use of normalized difference indices. A major drawback with this method is the spatial resolution of Landsat which is 30 meters after pan sharpening that cannot effectively monitor objects that are less than the sensors resolution [23].

Phiri et al. [19] studies the performance of various classifiers, namely: (Maximum Likelihood Classifier (MLC), Support Vector Machine (SVM), Classification Tree (CT), k Nearest Neighbor (k-NN) and Random Forest (RF)) in the production of LULC with the use of a Sentinel-2 dataset. There findings were that RF is a widely used classifier that obtained an Average Overall Accuracy > 90% when a Sentinel-2 dataset is used in their study [29].

The backscatter intensities of the combined water and feature clusters constitute a pair of Gamma densities for each component in the set of backscatter in which we observe (W+F), and the confluence of these two densities corresponds to a threshold that can minimize misclassification [37]. The Bayes Theorem is used to derive the local threshold $\sigma 0.t_N$ that is used to segregate water pixels (W) from other feature pixels (F), where the probabilities are functions of the backscattering coefficient $\sigma 0$ such that $P(W(\sigma 0))$ and $P(F(\sigma 0))$. As a result, equation 1 below appears.

$$\sigma 0.t_N = aeg\ \min\left|\frac{P(W(\sigma 0))}{P(F(\sigma 0)} - 1\right| \quad (1)$$

The lower limit of equation 1 above is reached at the backscatter intensity $\sigma 0.t_N$, where the posterior probabilities of water and feature cluster are identical [38]. We shall apply the local threshold $\sigma 0.t_N$ to the elements of (W + F) in order to distinguish the amount of water at each element in the set. Pixels in the subset are classed as water if the $\sigma 0$ value is below the threshold $\sigma 0.t_N$ and as other feature if they prove otherwise.

B. Research Questions and Hypotheses

This research introduces the use of a local threshold by SAR CD determined by manual histogram fitting to delineate flood extent that is viable for the study area Mumbwa based on the local backscatter of the terrain determined by the DEM. Thereafter the generated flood map using the LULC map produced by the classification of Sentinel-2 optical data by the use of a suitable machine learning classification algorithm. To this effect it is hypothesized that there exists a SAR histogram threshold $\sigma 0.t_N$ of the study area of Mumbwa determined by Elevation and Terrain structure which is heterogeneous in this case that can be determined and used to extract water features from the larger SAR dataset. Therefore, it is attempted to identify a suitable local backscattering coefficient threshold value for the study area that will intern be used in GEE to automate the production

of a flood maps in perpetuity as the region is flood prone. The research questions therefore are;

(1) In which range of values does the local backscattering coefficient threshold $\sigma 0.t_N$ for the study area of Mumbwa lie? And is the coefficient threshold value a Real or Complex number?

(2) Which classification algorithm will best suit the study area which is heterogeneous in landscape?

III. DATASETS

A. Study Area

The District of Mumbwa lies in the Central Province of The Republic Zambia with a land area of approximately 2,143,019 Hectares. It has several hydrological features including streams and rivers that do tend to experience seasonal flooding, particularly in the rainy season between December and May [13]. Approximately 3,000 people were displaced from their homes as a result of flooding in Mumbwa with total rainfall recorded of about 370.92 mm during the 2020–21 rainy season between December 2020 and May 2021.

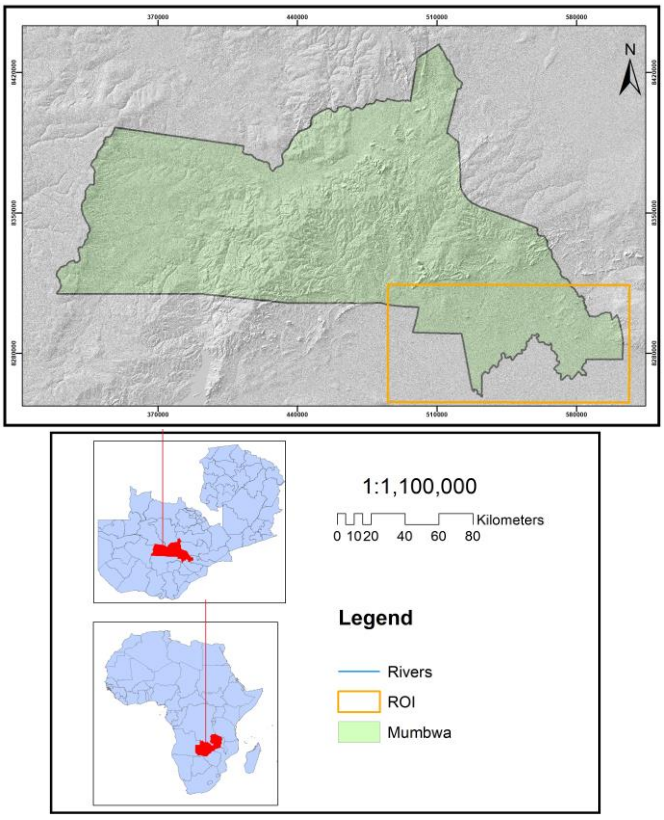

Fig. 1. *Site Plan of Study Area*

The region of interest for the study is located South East of the District of Mumbwa and is bordered by the Kafue River as shown in Figure 1 and has an area of 709,357 Hectares.

TABLE I. RAINFALL DATA FOR THE STUDY AREA

Month	***Rainfall (mm)***
2020 December	125.88
2021 January	85.4
2021 February	127.33
2021 March	25.51
2021 April	6.42
2021 May	0.38
TOTAL	**370.92**

During the rainy season under study, the months of December 2020 and February 2021 received the most rainfall. The study focused on the entirety of the rainy season to reduce and dilute the biases and errors in collection that may have occurred in the individual months [14].

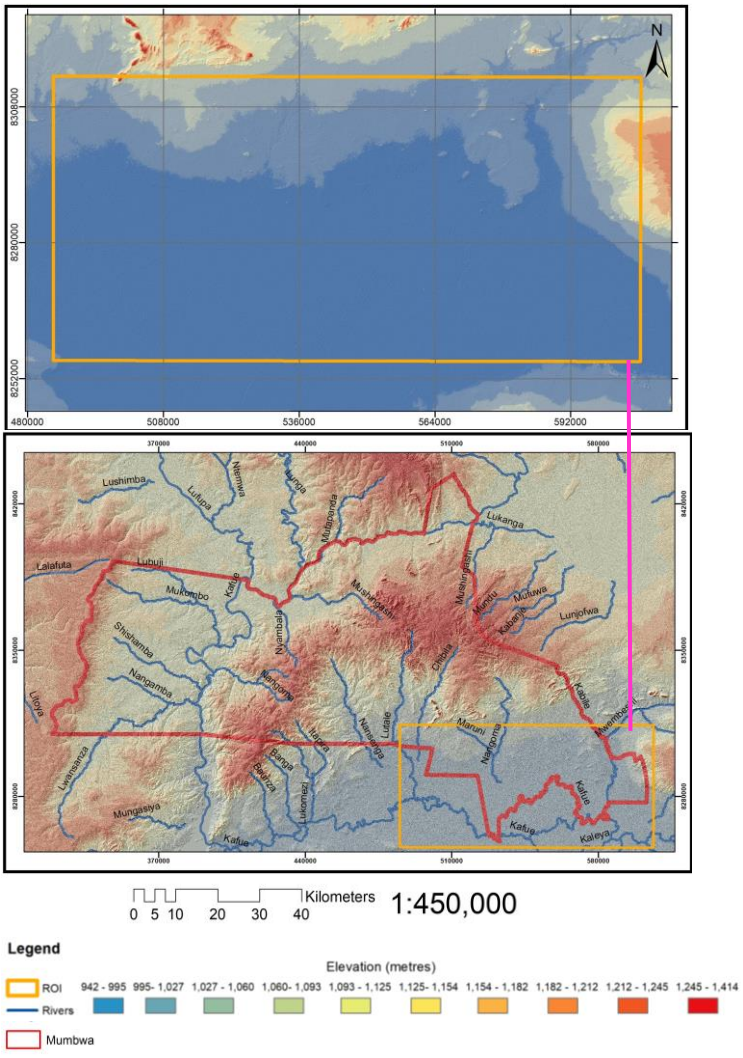

Fig. 2. *Digital Elevation Model (DEM) of the study area*

The study area as shown in Figure 2 lies in a depressed region in terms of elevation above mean sea level. The elevation values are between 942 to 1200 meters above sea level. The said region hosts several rivers and streams which are important for our study as flooding results in an overspill of the open water in these bodies.

B. *Datasets*

Sentinel-1 SAR Data

The satellite constellation is a SAR project that provides continuous C-band images in four modes with various geographic resolutions both during the day and night. It uses two satellites launched separately, Sentinel-1A and Sentinel-1B [15]. The image capture cycle takes 6 days when both spacecraft are used and 12 days when only one is used. It has a pre-planned monitoring scenario in place to ensure consistency and avoid conflict. To ensure a time series over land, the same SAR polarity technique is used [16]. For this study the Ground Range Detected (GRD) product was used. It has the polarizations VV and VH based on an Earth ellipsoid model, the product is constructed from identified, multi-looked, and ground range SAR data [17]. The mode for the GRD product is Interferometric Wide Swath (IW) that has a swath of and a spatial resolution of 5 x 20 m.

Sentinel-2 MSI

Two polar-orbiting satellites, Sentinel-2A and Sentinel-2B, each equipped with an optical imaging sensor MSI ((Multi-Spectral Instrument), make up the Sentinel-2 mission. On June 23, 2015, Sentinel-2A was launched and on March 7, 2017, Sentinel-2B [18]. It has a temporal resolution of 5 days at the equator if both constellation satellites are used and 10 days if only one satellite is used, the band specifications are shown in Table 2 [19].

TABLE II. SENTINEL-2 BAND SPECIFICATIONS

Spatial Resolution (m)	Bands	Central Wavelength (µm)
10	Band 2 - Blue	0.49
	Band 3 - Green	0.56
	Band 4 - Red	0.665
	Band 8 - NIR	0.842
20	Band 5 - Vegetation Red Edge	0.705
	Band 6 - Vegetation Red Edge	0.74
	Band 7 - Vegetation Red Edge	0.783
	Band 8A - Vegetation Red Edge	0.865
	Band 11 - SWIR	1.61
	Band 12 - SWIR	2.19
60	Band 1 - Coastal aerosol	0.443
	Band 9 - Water vapour	0.945
	Band 10 - SWIR - Cirrus	1.375

Digital Elevation Model (DEM)

To determine which regions over the study area will be inundated and retain flood water, a Digital Elevation Model (DEM) was of key importance as floods generally inundate regions with low slope values [20]. The HydroSHED dataset was used for this. It is a georeferenced dataset that is derived from elevation data from the Shuttle Radar Topography Mission (SRTM) at a spatial resolution of 3 arc-seconds (30 meters). It is comprised of watershed boundaries, stream networks, and other hydrological features [21].

Global Surface Water Mapping

Various indices exist for the mapping of open water features using optical datasets. These methods apply said indices over images to produce Surface Water datasets [22]. This study used such a dataset, particularly the Global Surface Water Dataset to differentiate between permanent water and flood water over the study area. The dataset uses millions of Landsat images over 32 years to delineate permanent water extent at a spatial resolution of 30 meters [23].

IV. METHODS AND PROCEDURES

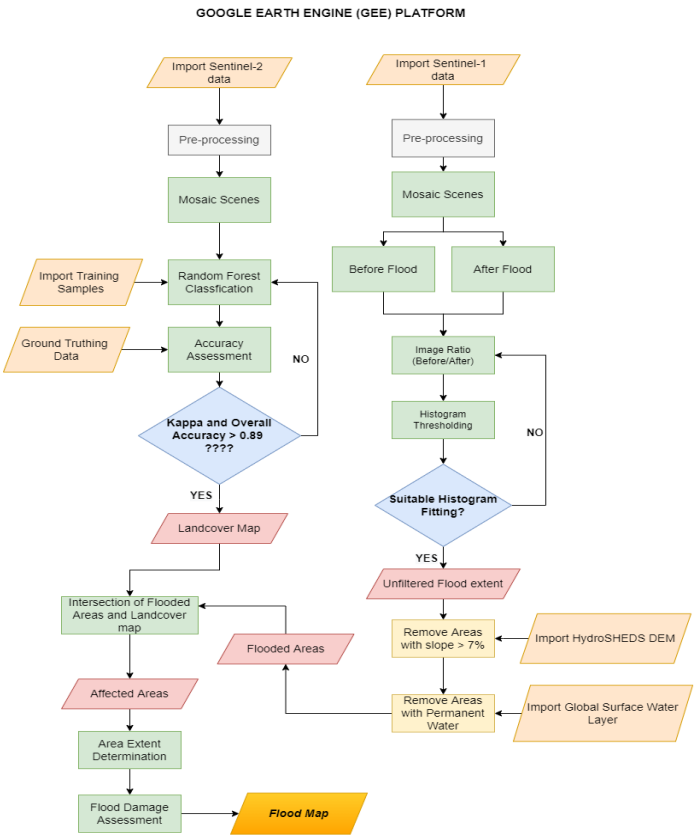

Fig. 3. *Flow Chart of Methodology*

A. Sentinel-1 Data Pre-Processing and Processing

Sentinel-1B SAR data was acquired and processed through the Google Earth Engine (GEE) platform. There are various approaches to disaster analysis and mitigation such as Multi-Criteria Decision Analysis (MCDA). This study, however, took the Change detection approach to work with the SAR data [24]. The selected images for the "*before flood*" period were a mosaic selected by a date filter from the dates 01-08-2020 to 31-08-2020 and for the "*after flood*" period the dates were also a mosaic for the dates 01-12-2020 to 31-05-2021. The mosaicking was applied to the images to produce two images, namely *the before* and *after* flood images, the pre-processing steps carried out were: *radiometric calibration, removal of noise from thermal sources, speckle filtering* and *terrain correction* [25]. All the pre and post-processing were done using GEE through the Java Script API [26]. The radiometric calibration converted intensity values to sigma naught (dB) which are the backscatter values needed for our analysis. The Polarization 'VH' was used as it is recommended for use in flood analysis due to its ability to show a sharp contrast between land and water-related pixels. The orbit for Sentinel-1B passing over Zambia follows an Ascending pass direction. The pre-processing was carried out starting with the speckle filter and using a smoothing radius of 50 meters applied to the images to remove salt and pepper noises from the images as it reduces the quality of the satellite imagery and the backscatter interpretation thereafter may be erroneous. The ellipsoid used in SAR products as the reference surface causes geometric distortions in the image and therefore terrain correction was carried out [27]. After the pre-processing was carried out, the change detection by image ratio was carried out. The before and after image mosaics were divided as per change detection ratio with a local histogram threshold $\sigma 0.t_N$ of 1.26 dB. The global threshold used for delineating water is 1.25 dB but for our study area, the value of 1.26 dB best produced a histogram fitted to water backscatter change. The resulting layer after the change detection by image ratio was then classified into two classes, where: the pixels correlating to water change were given a value of 1 whereas other feautures were given a value of 0 [28]. Thereafter, filtering of the initial flood extent was carried out. Primarily, the Global Surface Water Layer was used to clip out regions with permanent water that coincided with the flood water. Secondarily, the HydroSHEDS DEM was used to clip out regions with slope values greater than 7% as flood water tends to run off steep surfaces. Upon carrying out these processes, the output was the Flooded Areas layer as illustrated in Figure 6.

B. Sentinel-2 Data Pre-Processing and Processing

In order to adequately study and assess the flood impact, a LULC map of the study area was required and for this, Sentinel-2 was used [29]. The product used was Sentinel-2 Level-2A which has already undergone radiometric calibration and atmospheric correction. Radiometric Calibration is the process where Digital Number (DN) values that are recorded by the sensor are converted to top of atmosphere reflectance values, whereas atmospheric correction picks this up and converts the top of the atmosphere reflectance values to the bottom of atmospheric reflectance [30]. Therefore for our study, cloud masking was carried out in the GEE platform using the metadata. The cloud pixel percentage that was chosen was 20% implying that only images of that value or less were loaded for cloud masking and further processing. A mosaic by filter date was carried out for our study area with the overlap of the region of interest [31]. The image scenes were mosaicked and filtered between the dates 01-08-2020 and 30-08-2020, thereafter the Landcover classification commenced. The image mosaic was then stacked to the specific bands that were needed for this process and these were 'B2', 'B3', 'B4', 'B5', 'B6', 'B7', 'B8', 'B8A', 'B11' and 'B12' as Table II specifies. The loaded image in a stacked multiband mosaic was then trained using sample regions [32]. The Landcover classes that were considered were 8 in number, namely: *open water, bare soil, trees, built-up, shrubland, crop fields, wetland* and *biochar*. Points were used to pick training data in GEE over the study area of 1,345 regions of interest and these were the training samples used for the 8 classes [33]. These were noted in a ground truthing site visit and were observable classes in the study area. To pick the training data, colour composites were used in GEE and these were False Colour and True Colour Composites. Following this, the training samples were then passed to a Machine Learning Algorithm. Three (3) machine learning algorithms were tested for this and they were; *Support Vector Machine, Decision Trees (CART*) and *Random Forest (RF)*. For the final results, RF was used with 1,000 trees and the LULC map was produced [34]. Accuracy assessment was carried out for the three (3) machine learning classification algorithms using GEE functions and the outputs for error evaluation were; *producer accuracy*, *overall accuracy* and *Kappa (K) Coefficient* [35]. Iterations were carried out to produce a Landcover map of desirable accuracy meeting a Kappa and Overall accuracy greater than 0.89. Upon the production of such a map, it was then used with the flooded areas to conduct an accuracy assessment [36].

V. Results and Discussion

A. Land Use Land Cover Map

The LULC map produced in GEE by the stated methods is depicted in Figure 4. Various algorithms were used in the production of a desirable map for flood analysis. The satisfactory result that met the required criteria of $k > 0.89$ was the RF classification algorithm that had the subsequent results.

Several iterations were carried out with all other parameters constant and only the number of Trees in the RF was altered and the best result had 1000 trees. Table 3 shows how the various algorithms performed in terms of overall accuracy and kappa.

TABLE III. OVERALL ACCURACIES AND KAPPA COEFFICIENTS OF CLASSIFICATION ALGORITHMS USED

Algorithm	Overall Accuracy	Kappa
RF (1000 Trees)	0.95700	0.91519
RF (100 Trees)	0.95562	0.91246
Decision Tree	0.94036	0.88287
SVM (Voting)	0.83773	0.65465
SVM (Margin)	0.81137	0.59973

The LULC map after cleaning and post-processing produced an output shown in Figure 4. The eight Landcover classes in the study area are depicted visually and in Table 4, the areas in hectares are represented. A large share of 46.50% of the study area had biochar due to charcoal production in the study area. The classes of interest were Built-Up, Trees and Crop Fields which covered 0.27%, 5.18% and 1.03% respectively.

TABLE IV. LAND USE LAND COVER (LULC) MAP STATISTICS

Landcover	Pixel Count	Area (Ha)	Percentage
Open Water	1,964,925	18,913.53	2.67
Bare Soil	12,866,380	123,846.30	17.48
Trees	3,815,892	36,730.14	5.18
Built-Up	195,709	1,883.81	0.27
Shrubland	10,022,631	96,473.55	13.61
Crop Fields	761,621	7,331.04	1.03
Wetland	9,763,974	93,983.84	13.26
Biochar (Soil)	34,230,913	329,492.10	46.50
Total	**73,622,045**	**708,654.31**	**100**

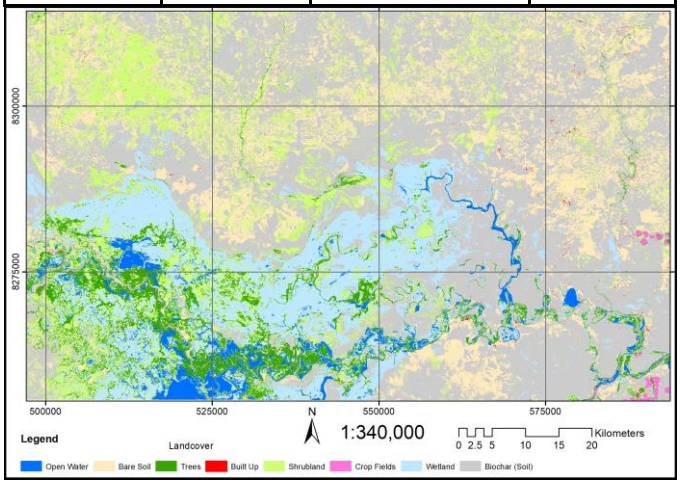

Fig. 4. *Land Use Land Cover (LULC) map of the study area for August 2020 using Sentinel-2A satellite imagery in GEE using RF Classification algorithm*

B. *Flood Extent*

The backscatter analysis based on the histogram values for the SAR imagery showed the plot fitting as in Figure 5. The *pre-flood* image showed intensity ranging from -35 to -5 dB whereas the *after-flood* showed a range of -33 to -3dB. Based on the skew of the graph it can be observed that the *before-flood* image mosaic had a limited number of pixels correlating to the backscatter of water. In the *after-flood* image, the skew at -21.01 dB correlates to backscatter resulting from water. The *after-flood* image shown in Figure 5(c) shows a histogram plot for the image ratio with a threshold of 1.26 dB which was chosen for the case study due to suitable histogram fitting. From this it can be observed that a significant amount of water was captured by this local histogram threshold.

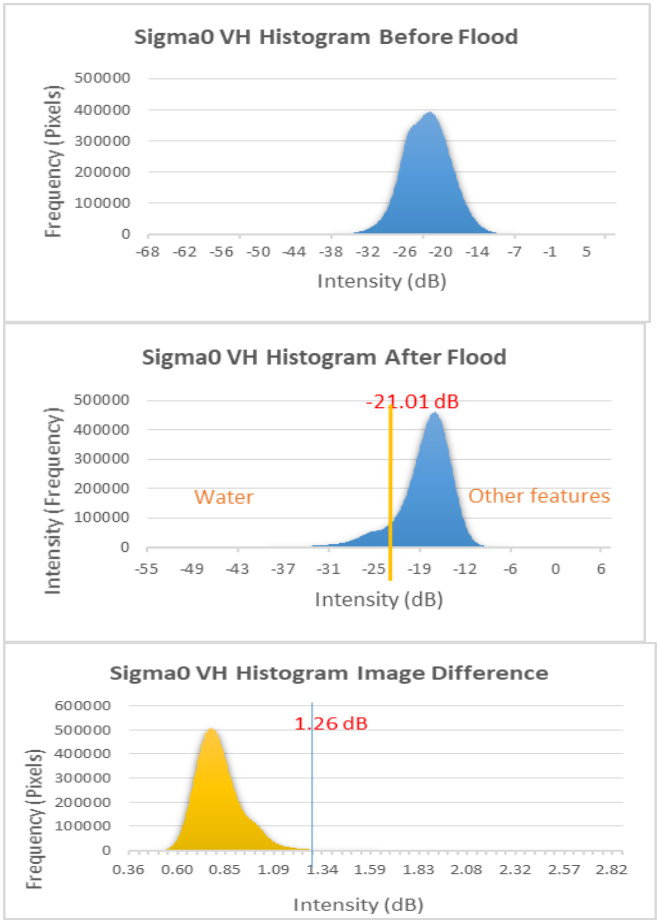

Fig. 5. *Plots of histograms of the (a)before flood period, (b)after flood and (c) ratio image difference*

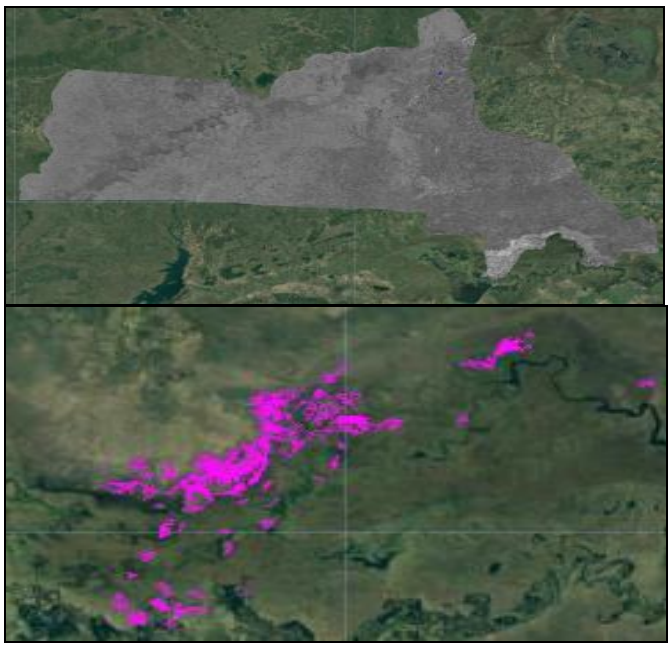

Fig. 6. *Image Ratio SAR result in GEE (a) Mumbwa Image difference over True Colour Composite (b) Flooded areas.*

Figure 6 above shows the result of the image ratio in a SAR image with backscatter correlating to water change as well as the flooded areas in GEE.

C. Flood Damage

In this study, *flood damage* was defined as the change of Landcover from an initial land class *before the flood* period to a water class in the *after-flood* period. The analysis therein resulted in the flood damage as shown in Table 5.

TABLE V. LANDCOVER DAMAGE TO CLASSES IN THE STUDY AREA

Landcover	Pixel Count	Area (Ha)	Percentage
Bare Soil	28,411	273.47	1.44
Trees	360,121	3,466.37	18.19
Built-Up	429	4.13	0.02
Shrubland	531,683	5,117.75	26.86
Crop Fields	19,811	190.69	1.00
Wetland	658,555	6,338.97	33.27
Biochar (Soil)	380,286	3,660.47	19.21
Total	**1,979,296**	**19,051.85**	**100**

The inital trend shows flood water to primarily displace wetlands noted by the 33.27% share in the affected landcover as is expected due to these regions lying in close proximity to open water bodies.

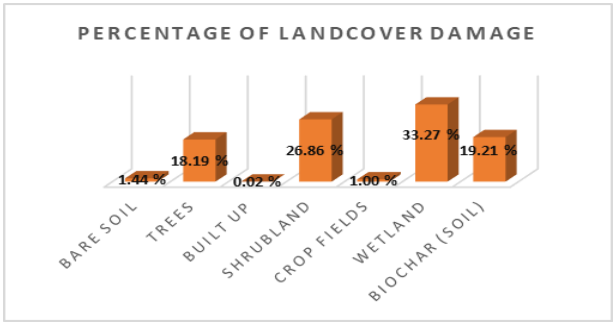

Fig. 7. *The percentage of landcover damage for the study area of Mumbwa*

The damage to Bulit-Up areas was found to be 0.02% and Crop Fields 1% whereas the flood damage to trees was 18.19%. The total flood extent was 19,051.85 Hectares which is 2.69 per cent of the land area under study in Mumbwa.

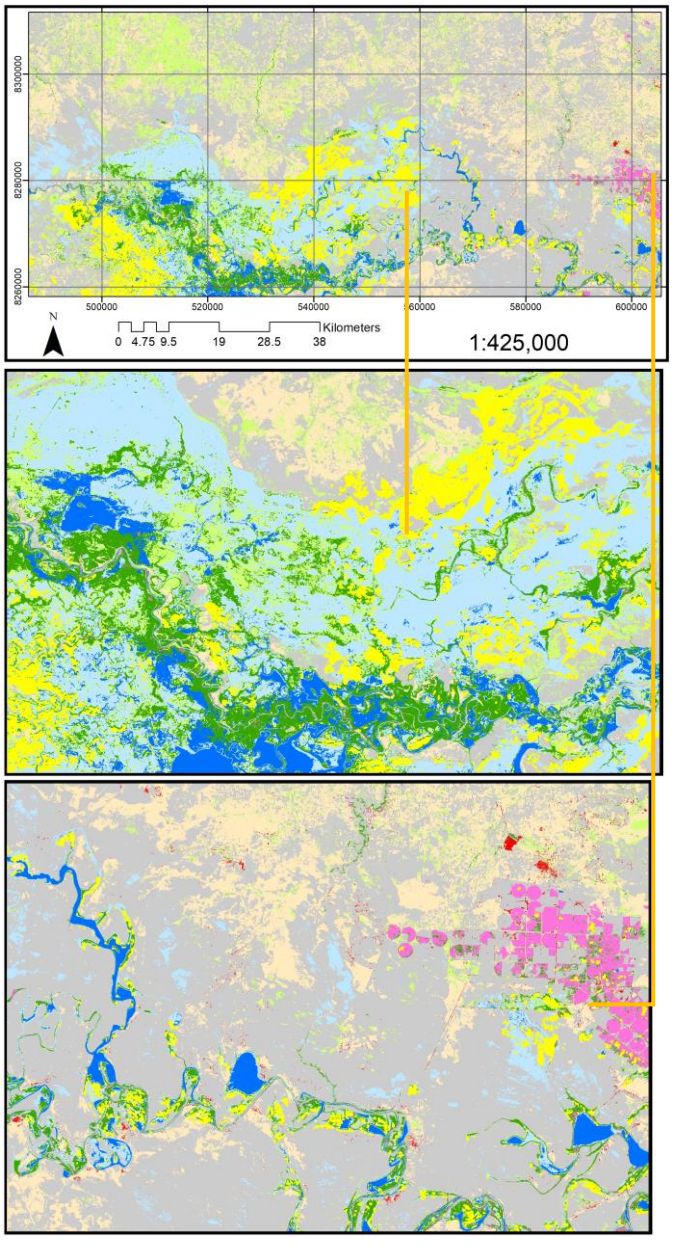

Fig. 8. *Flood Map of Mumbwa showing affected Landcover classes as the Map Legend specifies.*

VI. CONCLUSION

The Mumbwa Flood of December 2020 was investigated within the region of study located South-East of the District. The method of analysis was novel as it used a local histogram threshold $\sigma 0.t_N$ of Sentinel-1B SAR data of 1.26 dB which is a real number and fits the terrain of the study area which is heterogeneous and allows for better backscatter analysis as opposed to the global threshold of 1.25 dB and thus the first research question was answered. The change detection approach was utilized by image ratio for the *before-flood* image mosaic dated August 2020 and the *after-flood* mosaic of 01-12-2020 to 31-05-2021. In order to eliminate regions that have slopes over 7% which runoff during flood times, these were clipped out of the resulting flood extent. Furthermore, regions with permanent water were also removed from the flood inundation extent by the use of the Global Surface Water Layer, resulting in the *flood extent map*. To carry out damage assessment it was necessary to produce a Landcover map of accuracy k > 0.89 and this was done using the *Random Forest classification algorithm* in GEE with 1000 trees that scored a k = 0.915. The Landcover map had the classes: *Open water*, *Bare Soil*, *Trees*, *Built Up*, *Shrubland*, *Crop Fields*, *Wet Land* and *Biochar*. Thereafter, the flood damage analysis was carried out by superimposing the flood extent over the Landcover map and clipping the two layers. This resulted in the *Landcover damage* which showed damage of 19,051.85 Hectares. Of this, the damage to Built-Up and crop fields was 0.02% and 1%, respectively. Therefore the hypothesis of the existence of a *Real* histogram threshold backscatter coefficient specifically suited to the study area of Mumbwa was proven to be true. The workflow allows for automation of future flood analysis utilizing the applied histogram threshold when a study region of similar terrain is investigated.

REFERENCES

[1] F. Conde, and M. De Mata Muñoz, "Flood Monitoring Based on the Study of Sentinel-1 SAR Images: The Ebro River Case Study," in Water, vol. 11 no. 12, 2019, pp. 2454.

[2] S. Long, T. Fatoyinbo and F. Policelli, "Flood Extent Mapping for Namibia Using Change Detection and Thresholding with SAR," in Environmental Research Letters, vol. 9, 2014.

[3] C. Li, Z. Ma, L. Wang, W. Yu, D. Tan, B. Gao, Q. Feng, H. Guo and Y. Zhao, "Improving the Accuracy of Land Cover Mapping by Distributing Training Samples," in Remote Sensing vol. 13 i=no. 12, 2021, pp. 4594.

[4] Z. Xu, J. Chen, J. Xia, P. Du, H. Zheng and L. Gan, "Multisource Earth Observation Data for Land-Cover Classification Using Random Forest," in IEEE Geoscience and Remote Sensing Letters, vol. 15, no. 5, 2018, pp. 789-793.

[5] M. Chini, R. Hostache, L. Giustarini and P. Matgen, "A Hierarchical Split-Based Approach for Parametric Thresholding of SAR Images: Flood Inundation as a Test Case," in IEEE Transactions on Geoscience and Remote Sensing, vol. 55 no. 12, 2017, pp. 6975-6988.

[6] N. A. Muhadi, A. F. Abdullah, S. K. Bejo, M. R. Mahadi and A. Mijic, "The Use of LiDAR-Derived DEM in Flood Applications: A Review," in Remote Sensing, vol. 12 no. 14, 2020, pp. 2308.

[7] O. Mutanga and L. Kumar, "Google Earth Engine Applications," in Remote Sensing, vol. 11, 2019, pp. 591.

[8] P. Lal, A. Prakash and A. Kumar, "Google Earth Engine for Concurrent Flood Monitoring in the Lower Basin of Indo-Gangetic-Brahmaputra Plains," In Natural Hazards, no. 104, 2020, pp. 1947–1952.

[9] S. Adeli, B. Salehi, M. Mahdianpari, L. J. Quackenbush, B. Brisco, H. Tamiminia and S. Shaw, "Wetland Monitoring Using SAR Data: A Meta-Analysis and Comprehensive Review," in Remote Sensin, vol. 12, 2020, pp. 2190.

[10] W. Mukupa, "Change detection and deformation monitoring of concrete structures using terrestrial laser scanning," University of Nottingham, Nottingham, 2017.

[11] H. A. Afify, "Evaluation of Change Detection Techniques for Monitoring Land-Cover Changes: A Case Study in New Burg El-Arab Area," In Alexanria Engineering Journal, vol. 50 no. 2, 2011, pp. 187-195.

[12] D. Moraes, P. Benevides, H. Costa, F. D. Moreira and M. Caetano, "Influence of Sample Size in Land Cover Classification Accuracy Using Random Forest and Sentinel-2 Data in Portugal," in IEEE International Geoscience and Remote Sensing Symposium, 2021, pp. 4232-4235.

[13] L. Milani, J. Lehmann, K. V. Naydenov, K. Saalmann, P. A. M. Nex, J. A. Kinnaird, I. S. Friedman, T. Woolrych and D. Selley, "Geology and Mineralization of the Cu-rich Mumbwa District, a Potential IOCG-type System at the Eastern Margin of the Pan-African Hook Batholith, Zambia," in Journal of African Earth Sciences, vol. 158, 2019.

[14] H. Ashouri, K. Hsu, S. Sorooshian, D. K. Braithwaite, K. R. Knapp, L. D. Cecil, B. R. Nelson and O. P. Prat, "PERSIANN-CDR: Daily Precipitation Climate Data Record from Multisatellite Observations for Hydrological and Climate Studies," in Bulletin of the American Meteorological Society, vol. 96 no. 1, 2015, pp. 69-83.

[15] A. Flores, K. Herndon, R. B. Thapa, and E. A. Cherrington, The Synthetic Aperture Radar (SAR) Handbook: Comprehensive Methodologies for Forest Monitoring and Biomass Estimation, NASA, Washington D. C., 2019, pp. 216-290.

[16] R. Torres, P. Snoeij, D. Geudtner, D. Bibby, M. Davidson, E. Attema, P. Potin, B. Rommen, N. Floury, M. Brown, I. N. Traver, P. Deghaye, B. Duesmann, B. Rosich, N. Miranda, C. Bruno, M. L'Abbate, R. Croci, A. Pietropaolo, M. Huchler and F. Rostan, "GMES Sentinel-1 mission," in Remote Sensing of Environment vol. 120, 2012, pp. 9-24.

[17] F. Filipponi, "Sentinel-1 GRD Preprocessing Workflow," in Proceedings, vol. 18, 2019, pp. 11.

[18] M. Main-Knorn, B. Pflug, J. Louis, V. Debaecker, U. Müller-Wilm and F. Gascon, "Sen2Cor for Sentinel-2," in Proceedings of SPIE 10427 Image and Signal Processing for Remote Sensing XXIII, 2017.

[19] D. Phiri, M. Simwanda, S. Salekin, V. R. Nyirenda, Y. Murayama, M. Ranagalage, "Sentinel-2 Data for Land Cover/Use Mapping: A Review," in Remote Sensing, vol. 12, 2020, pp. 2291.

[20] A. B.Wickel, B. Lehner and N. Sindorf, "HydroSHEDS: A Global Comprehensive Hydrographic Dataset," in AGU Fall Meeting Abstracts, 2007, pp. 1800-1850.

[21] T. R. da Costa, P. Mazzoli, S. Bagli. Limitations Posed by Free DEMs in Watershed Studies: The Case of River Tanaro in Italy", in Frontiers in Earth Science, ed. 7, 2019, pp 3389-3395.

[22] Y. Zhou, J. Dong, X. Xiao, T. Xiao, Z. Yang, G. Zhao, Z. Zou and Y. Qin, "Open Surface Water Mapping Algorithms: A Comparison of Water-Related Spectral Indices and Sensors," in Water, vol. 9, 2017, pp. 256.

[23] J. Pekel, A. Cottam, N. Gorelick and A. S. Belward, "High-Resolution Mapping of Global Surface Water and its Long-Term Changes," in Nature, vol. 540, 2016, pp. 418-422.

[24] P. H. Nyimbili, T. Erden and H. Karaman, "Integration of GIS. AHP and TOPSOS for Earthquake Harzard Analysis," in Natural Hazards, vol. 92, 2018, pp. 1523-1546.

[25] A. C. Pandey, K. Kaushik and B. R. Parida, "Google Earth Engine for Large-Scale Flood Mapping Using SAR Data and Impact Assessment on Agriculture and Population of Ganga-Brahmaputra Basin," in Sustainability, vol. 14 no. 12, 2022 pp. 4210.

[26] G. Moser and S. B. Serpico, "Generalized Minimum-Error Thresholding for Unsupervised Change Detection from SAR Amplitude Imagery," in IEEE Transactions on Geoscience and Remote Sensing, vol. 44, no. 10, 2006, pp. 2972-2982.

[27] F. Bioresita, N. Hayati, M. G. R. Ngurawan and M. Berliana, "Integrating InSAR Coherence and Backscattering for Identification of Temporary Surface Water, Case study: South Kalimantan Flooding, Indonesia," in The International Archives of Photogrammetry, Remote Sensing and Spatial Information Sciences; Gottingen, vol. XLIII-B3-2022, 2022, pp. 33-39.

[28] M. N. Sumaiya and R. S. S. Kumari, "Logarithmic Mean-Based Thresholding for SAR Image Change Detection," in IEEE Geoscience and Remote Sensing Letters, vol. 13 no. 11, 2016, pp. 1726-1728.

[29] T. N. Phan and M. Kappas, "Comparison of Random Forest, k-Nearest Neighbor, and Support Vector Machine Classifiers for Land Cover Classification Using Sentinel-2 Imagery" in *Sensors, vol.* 18 no. 1, 2018, pp. 18.

[30] A. M. Abdi, "Land Cover and Land Use Classification Performance of Machine Learning Algorithms in a Boreal Landscape using Sentinel-2 Data," in GIScience & Remote Sensing, vol. 57 no. 1, 2020, pp. 1-20.

[31] H. Zheng, P. Du, J. Chen, J. Xia, E. Li, Z. Xu, X. Li and N. Yokoya, "Performance Evaluation of Downscaling Sentinel-2 Imagery for Land Use and Land Cover Classification by Spectral-Spatial Features," in *Remote Sensing*, vol. 9 no. 12, 2017, pp. 1274.

[32] R. Malinowski, S. Lewiński, M. Rybicki, E. Gromny, M. Jenerowicz, M. Krupiński, A. Nowakowski, C. Wojtkowski, M. Krupiński, E. Krätzschmar and P. Schauer, "Automated Production of a Land Cover/Use Map of Europe Based on Sentinel-2 Imagery," in *Remote Sensing*, vol. *12* no. 21, 2020, pp. 3523.

[33] B. Hu, Y. Xu, X. Huang, Q. Cheng, Q. Ding, L. Bai and Y. Li, "Improving Urban Land Cover Classification with Combined use of Sentinel-2 and Sentinel-1 Imagery", in *ISPRS International Journal of Geo-Information*, vol. *10* no. 8, 2021, pp. 533.

[34] C. Cortes, and V. Vapnik, "Support-Vector Networks," in *Macbine Learning*, vol. 20 no. 3, 1995, pp. 273-297.

[35] G. Mountrakis, J. Im, and C. Ogole, "Support Vector Machines in Remote Sensing: A review," in *ISPRS Journal of Photogrammetry and Remote Sensing, vol.* 66 no. 3, 2011, pp. 247-259.

[36] J. H. Friedman, "Greedy Function Approximation: A Gradient Boosting Machine," in *Annals of statistics, vol. 29 no. 5*, 2001, pp. 1189-1232.

[37] H. W. Chung, C. C. Liu, I. F. Cheng, Y. Y. Lee and M. C. Shieh, "Rapid Response to a Typhoon-Induced Flood with an SAR-Derived Map of Inundated Areas: Case Study and Validation" in Remote Sensing, Vol. 7 no 9, 2015, pp 11954-11973.

[38] J. Liang and D. Liu, "A Local Thresholding Approach to Flood Water Delineation Using Sentinel-1 SAR Imagery" in ISPRS Journal of Photogrammetry and Remote Sensing, Issue 159, 2020, pp 53-62.